PAPER

Carbon-coated α-Fe₂O₃ nanostructures for efficient anode of Li-ion battery†

Xiaoxin Lv,[a] Jiujun Deng,[a] Jian Wang,[b] Jun Zhong*[a] and Xuhui Sun*[a]

Carbon-coated α-Fe₂O₃ nanostructures, as the anode of Li-ion battery, have been deposited on the stainless steel substrate by a facile pyrolysis of ferrocene. The anode shows a high reversible capacity of 1138 mA h g⁻¹ after 300 cycles at the current density of 500 mA g⁻¹ and maintains a good capacity of 458.8 mA h g⁻¹ even when cycled at the high current density of 10 000 mA g⁻¹. This high capacity can be associated to the nanostructure and the carbon layer coated on hematite. Moreover, the mechanism for the capacity evolution with cycling has been investigated by scanning transmission X-ray microscopy (STXM). The results reveal that the detailed composition and electronic structure change in the cycling process. Fe chemical state plays a critical role in the capacity evolution and a low oxidation state of Fe (such as Fe²⁺) might reduce the capacity by trapping Li⁺ ions, and the recovery of Fe²⁺ to hematite (Fe³⁺) significantly enhances the capacity. Data also show the growth and inhomogeneous distribution of a solid electrolyte interphase (SEI) layer containing carbon-based film, Li₂O and Li₂CO₃. The facile synthesis of carbon-coated α-Fe₂O₃ opens an efficient way for large-scale anode production of Li-ion batteries, and the STXM study provides new insights into the mechanism of hematite-based Li-ion battery.

Introduction

In the past decades, rechargeable lithium-ion batteries (LIBs) have been considered as the most promising energy storage system because of their high energy density, long lifetime, low self-discharge and environmental benignity.[1] Currently, the commercial anodes of LIBs are made of graphite. However, its lower theoretical capacity (372 mA h g⁻¹) and operating voltage limit the practical applications of LIBs in high power fields.[2,3] To meet the demands for high energy density batteries, it is essential to develop new electrodes from durable, low cost and environmentally benign materials to replace the graphite. With the advantages of its high theoretical capacity (1007 mA h g⁻¹), high corrosion resistance, abundant, nontoxicity and low processing cost, hematite (α-Fe₂O₃) has been regarded as one of the most promising anode materials.[4] However, it shows some drawbacks, such as fast capacity fading and bad rate capability during electrochemical cycling. Enormous efforts have been made to address these problems and improve the electrochemical performance of hematite electrodes.[5,6] One effective strategy is to coat iron oxide with carbon materials, which have good chemical stability and a wide electrochemically stable window in organic electrolytes to limit the surface degradation of electrode materials. Thus, carbon coating can effectively avoid the fast fading of the capacity and improve the cycling performance.[7–13]

Ferrocene has been reported to be a good precursor for hematite synthesis *via* a simple pyrolysis.[14,15] In this report, we have developed a simple approach to prepare the carbon-coated α-Fe₂O₃ nanostructures, which directly grow on the stainless steel (SS) *via* the pyrolysis of ferrocene as the anode of LIBs. The anode of carbon-coated α-Fe₂O₃ nanostructure shows a high reversible capacity of 1138 mA h g⁻¹ after 300 cycles at a current density of 500 mA g⁻¹. Moreover, the composition and electronic structure of the anode material with cycling have been probed by scanning transmission X-ray microscopy (STXM), which provides a new insight into the mechanism for the capacity evolution during the cycling.

Scanning transmission X-ray microscopy (STXM) is an effective tool to characterize the electronic structure of nanosystems.[16,17] STXM combines both X-ray absorption near-edge structure (XANES) spectroscopy and microscopy with a spatial resolution of a few tens of nanometers.[16,17] XANES is an element-specific spectroscopic technique involving the excitation of electrons from a core level to local and partial empty states of a defined character, which is also a useful tool to probe the interfacial interaction and charge transfer in the composites.[18,19] XANES has been widely used to probe the electronic structure evolution in LIBs.[20,21] STXM was also used to show the

ᵃSoochow University–Western University Centre for Synchrotron Radiation Research, Jiangsu Key Laboratory for Carbon-Based Functional Materials and Devices, Institute of Functional Nano and Soft Materials Laboratory (FUNSOM), Soochow University, Suzhou, China. E-mail: xhsun@suda.edu.cn; jzhong@suda.edu.cn

ᵇCanadian Light Source Inc., University of Saskatchewan, Saskatoon, SK S7N 0X4, Canada

† Electronic supplementary information (ESI) available: XRD data, TEM image with low magnification, XPS data and cycling performance of carbon-coated hematite. See DOI: 10.1039/c4ta06415a

visualization of the state of charge (SOC) in an $LiMn_{0.75}Fe_{0.25}$-PO_4 nanorods–graphene hybrid nanostructure in LIBs.[22] However, to the best of our knowledge, it is the first report of using STXM to investigate the electronic structure of hematite-based anode in the cycling process. The STXM data offer the details on the electronic structure evolution of the hematite-based anode materials with cycling. The results reveal that the capacity evolution could be related to the chemical state changes of Fe in the anode. Data also show the slow growth and inhomogeneous distribution of solid electrolyte interphase (SEI) layer, which consists of a carbon-based film, Li_2O and Li_2CO_3.

Experimental section

Preparation of α-Fe_2O_3 anodes

The stainless steel (SS) (304, 500 μm) discs were cleaned with acetone, ethanol and deionized water and then placed on the bottom of the glass culture dish around the ferrocene (0.3 g, J & K Scientific, 99%), which was in the centre of the container (Fig. 1). The glass culture dish was covered by a glass cover. After sintered at 550 °C for 2 hours in the muffle furnace, a layer of orange colour film could be found on the SS disc.

Structural characterization

The morphology of carbon-coated α-Fe_2O_3 nanostructures was characterized by scanning electron microscopy (SEM, FEI-quanta 200 with an acceleration voltage of 20 kV). Transmission electron microscopy (TEM, FEI Quanta FRG 200F, operating at 200 kV) equipped with energy dispersive X-ray analysis (EDX) spectroscopy was employed for the detail structural characterization. X-ray Diffraction (XRD, PANalytical, Zmpyrean) and X-ray photoelectron spectroscopy (XPS, Kratos AXIS UltraDLD) were also used to investigate the crystal structure and chemical state of the samples, respectively.

STXM experiment was performed on the SM beamline at the Canadian Light Source (CLS). Anode materials before cycling and after 1, 15 and 250 cycles (at a current density of 500 mA g^{-1}) were scratched from the substrate and sonically dispersed on TEM grid for STXM experiments. Before the experiments, the samples were characterized by TEM. The image sequence (stack) scans over a range of photon energies have been used to obtain both chemically contrast imaging and XANES spectra.[16,17] STXM data were analyzed by aXis2000 software (http://unicorn.mcmaster.ca/aXis2000.html).
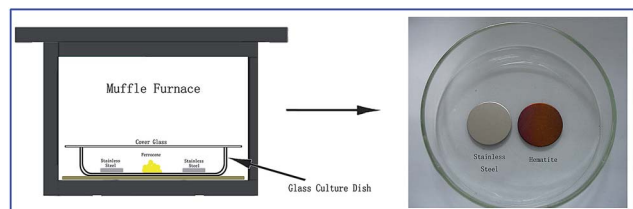

Fig. 1 Schematic illustration of the experimental set up (left panel) and an image of the stainless steel before and after sintering (right panel).

Electrochemical measurements

The electrochemical performance was characterized with CR2016 coin type half cells that were assembled in an Ar filled glove box (Mbraun, Labstar, Germany), using a multichannel battery tester (LAND CT2001A model, China). The assembled cell contains the nanostructured carbon-coated α-Fe_2O_3 directly grown on a SS disc as the anode, Li foil (0.59 mm thick, 14 mm diameter, China Energy Lithium Co., LTD.) as both the counter and reference electrodes, 1 M solution of $LiPF_6$ in ethylene carbonate (EC), diethyl carbonate membrane (DEC) as electrolyte, and Celgard 2325 as the separator. No conducting carbon and binder were used for the fabrication of the electrode. The amount of active materials on the SS disc was *ca.* 0.2 mg. The charge–discharge experiments were performed at different rates in the voltage range of 0.01–3.00 V. Cyclic voltammetry curves were tested using a CHI660D electrochemical workstation in the voltage range of 0.01–3.00 V at 0.2 mV s^{-1}.

Results and discussion

Ferrocene is an air-stable orange solid with the melting and boiling points of 172.5 °C and 249 °C, respectively. When the temperature is higher than 400 °C, ferrocene can be readily sublimed and forms the hematite *via* oxidation in air.[23] A previous study has found that a thin carbon layer can be formed on the surface of hematite nanostructures during the pyrolysis of ferrocene under the condition of insufficient oxygen content.[15] In this work, by the simple pyrolysis of ferrocene in a covered dish, carbon-coated hematite nanostructures were directly grown on SS. The image of the SS disc before and after the pyrolysis of ferrocene at 550 °C for 2 hours is shown at the right panel of Fig. 1. It is clear that the hematite films (orange color) were formed on the surface of SS disc. XRD data of the product is shown in Fig. S1 (ESI†), which can be indexed to the characteristic peaks of typical α-Fe_2O_3 (JCPDS 33-0664) after subtracting the substrate peaks.

Fig. 2(a) and (b) show the SEM images of α-Fe_2O_3 nanostructures obtained on the SS substrate, which exhibit a uniform morphology. The thickness of the α-Fe_2O_3 nanostructure film recorded by the cross-section SEM image in Fig. S2 (ESI†) is about 200 nm. TEM image of carbon-coated α-Fe_2O_3 with low magnification is shown in Fig. S3 (ESI†), and it shows that the average size of nanostructures is less than 50 nm. Fig. 2(c) is the high-resolution transmission electron microscope (HRTEM) image of the sample. A uniform carbon layer with a thickness of ~3 nm can be observed on the surface of α-Fe_2O_3 in the HRTEM image. The carbon layer shows the graphitic like layer structure. From the fast Fourier transform (FFT) of the lattice image of the carbon-coated α-Fe_2O_3, shown in Fig. 2(d), we can conclude that the α-Fe_2O_3 nanostructure is a single crystal with a lattice space of 0.27 nm, which stands for the (104) plane of α-Fe_2O_3. In Fig. 3, the elemental mapping and EDX spectrum of the α-Fe_2O_3 nanostructures are also shown. It clearly demonstrates that a thin carbon layer is uniformly coated on the surface of α-Fe_2O_3 nanostructures, which is in

5184 | *J. Mater. Chem. A*, 2015, **3**, 5183–5188

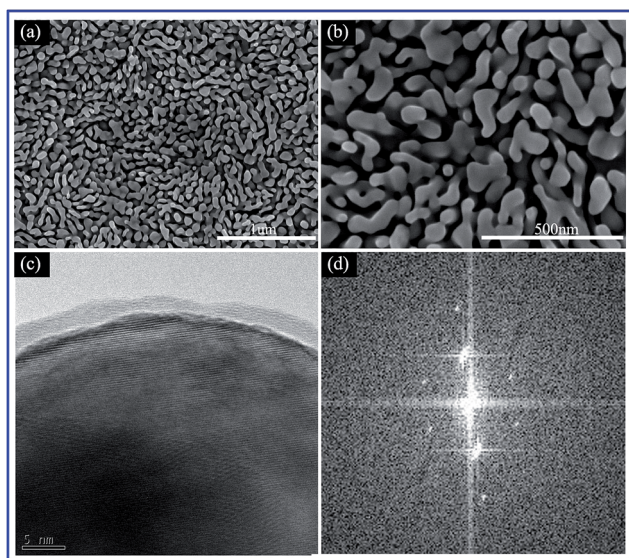This journal is © The Royal Society of Chemistry 2015

Fig. 2 (a) SEM image of α-Fe₂O₃ nanostructures on SS. (b) SEM image of α-Fe₂O₃ nanostructures on SS with higher magnification. (c) HRTEM image of α-Fe₂O₃. (d) Fast Fourier transformation pattern of the HRTEM image of carbon-coated α-Fe₂O₃ nanostructure in (c).
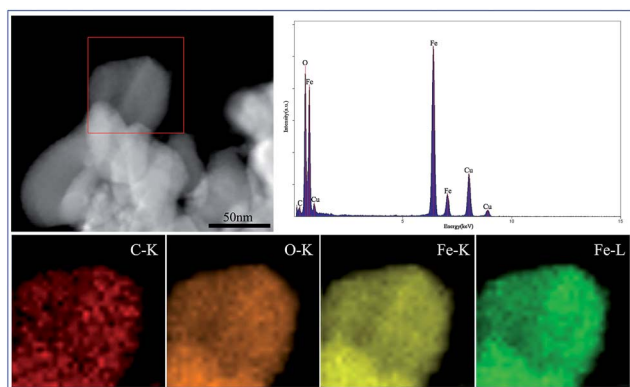

Fig. 3 Elemental mapping of carbon-coated α-Fe₂O₃ nanostructures: C (red), O (orange) and Fe (K-edge, yellow and L-edge, green) distribution in the selected area (red rectangle marked area in the left panel). The right panel shows the EDX spectrum of the selected area.

good agreement with the HRTEM image. The EDX data indicates that the weight content of carbon is about 1.3%.

XPS has also been employed to further clarify the composition of carbon-coated α-Fe₂O₃ nanostructures. XPS spectra of the samples are shown in Fig. S4 (ESI†). The XPS survey spectrum (Fig. S4(a)†) shows the peaks for Fe and O and an evident peak for the existence of C, further confirming the presence of carbon coating. The Fe 2p XPS spectrum (Fig. S4(b)†) shows two peaks at 711.6 eV and 724.4 eV, which correspond to Fe $2p_{3/2}$ and $2p_{1/2}$ core level in α-Fe₂O₃, respectively. The O 1s spectrum in Fig. S4(c)† shows one peak at 530.2 eV, corresponding to the O 1s in α-Fe₂O₃ and the other peak at around 532.0 eV as a result of the chemisorption of oxygen or water on the sample surface. The peak at 284.9 eV in C 1s XPS spectrum, shown in Fig. S4(d),†

could be attributed to the C–C bond (sp^2) of the carbon layer on the α-Fe₂O₃ nanostructure.

The electrochemical performance of carbon-coated α-Fe₂O₃ as the anode without any binder and conductive additive for LIBs is shown in Fig. 4. The cyclic voltammetry (CV) curves of the sample were recorded between 0.01 V and 3.00 V at a scan rate of 0.2 mV s⁻¹. The initial three cycles of CV curves are shown in Fig. 4(a). In the first cycle, there are three cathodic current peaks at 1.63 V, 0.92 V and 0.58 V related to different lithiation steps and the decomposition of electrolyte (also the formation of the SEI layer).[24–26] Two broad overlapping anodic peaks can also be observed between 1.5 and 2.0 V in the first cycle, which can be attributed to the oxidation of Fe to Fe^{2+} and the further oxidation to Fe^{3+} (Fe_2O_3).[24,27,28] In the subsequent cycles, the main broad cathodic peak shifts from 0.58 V to 0.85 V and the peak intensity decreases significantly, indicating that capacity loss and some irreversible processes occurred in the first cycle.[28] The anodic peaks also slightly shift in the subsequent cycles.[28,29] After the second cycle, the intensities of the peaks remain almost the same, indicating good stability during the discharge–charge processes.[28]

Fig. 4(b) shows the discharge–charge voltage profiles of the samples in the initial three cycles at a rate of 0.5 C (1 C is defined as 1000 mA g⁻¹) between 0.01 V and 3.0 V. The initial high discharge and charge capacities of 1166 and 861 mA h g⁻¹ are obtained with a coulombic efficiency of 73.8% in the first cycle. In the second cycle, the coulombic efficiency increases to 96%. As shown in Fig. 4(c), the cyclic stability of the sample is evaluated at a rate of 0.5 C between 0.01 and 3.0 V. Even after 300 cycles, the sample still keeps a high reversible discharge capacity of 1138 mA h g⁻¹, which leads to a high reversible capacity retention of 97.6%. Conspicuously, the carbon-coated α-Fe₂O₃ anode shows a superior discharge–charge cycling
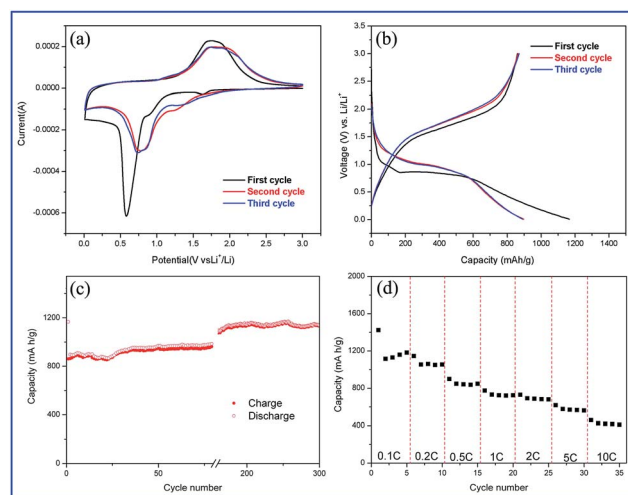

Fig. 4 (a) CV curves of carbon-coated α-Fe₂O₃ at a scan rate of 0.2 mV s⁻¹ for the initial three cycles between 0.01 and 3.0 V. (b) Discharge–charge voltage profiles of carbon-coated α-Fe₂O₃ electrode for the initial three cycles at a rate of 0.5 C between 0.01 and 3.0 V. (c) Cycling performance of carbon-coated α-Fe₂O₃ electrode at the rate of 0.5 C between 0.01 and 3.0 V. (d) Rate performance of carbon-coated α-Fe₂O₃ electrode at different current rates between 0.01 and 3.0 V.

stability. Moreover, the capacity gradually increases with cycling, and this phenomenon can be observed in other rates (shown in Fig. S5 (ESI†)). This phenomenon is attributed to the growth of a polymeric gel-like film (PGF), as reported in previous studies.[28,30–32]

To further investigate the rate capacity of carbon-coated α-Fe$_2$O$_3$ electrode, the electrode has been evaluated at different rates between 0.01 V and 3.0 V, and the results are shown in Fig. 4(d). At the rate of 0.1 C, the discharge capacity reaches 1182 mA h g^{-1}. Even at the higher rates of 1 C, 2 C, 5 C and 10 C, the discharge capacities still remains high at 774.2, 730.8, 618.1 and 458.8 mA h g^{-1}, respectively.

The superior reversibly high capacity of carbon-coated α-Fe$_2$O$_3$ can be attributed to several factors involving the unique morphology of the sample. The hematite consists of nanostructures, which may decrease the traverse time for electrons and Li$^+$ ions and then reduce the volume expansion during discharge–charge processes.[33] The carbon coating can enhance the conductivity and buffer the volume change of the active materials, which result in improved cycling performance and cycle life.[34,35] Both the carbon coating and the nanostructure of hematite could contribute to the high performance of the carbon-coated α-Fe$_2$O$_3$ anode.

To further understand the working mechanism of the hematite anode in the cycling process, we performed STXM experiments to reveal the composition and electronic structure changes in various steps of the cycling process. Anode materials before cycling and after 1, 15 and 250 cycles at 0.5 C were scratched from the SS and sonically dispersed on TEM grid for STXM experiments. STXM experiments at Fe L-edge, C K-edge, and O K-edge were carried out. For the samples before cycling and after 1 cycle, the compositions are almost uniform after analyzing the XANES spectra by pixel (about 30 nm) in the detected region (about 2 × 2 μm^2). However, for samples after 15 and 250 cycles, the compositions show inhomogeneous distribution with the aggregation of Li$_2$CO$_3$ or Li$_2$O. We thus show the colorful mapping and TEM images of various compositions in Fig. 5(a)–(f) for samples after 15 and 250 cycles, respectively. The corresponding XANES spectra of the different parts are also identified in Fig. 5(g)–(i).

Fe L-edge XANES spectra of the anode materials are shown in Fig. 5(g). The sample before cycling (black) shows a typical spectral shape for hematite with two main features at about 706–710 eV and 720–725 eV for Fe L$_3$ and L$_2$-edge resonances, respectively. However, the intensity ratio of peak at 707 eV (labeled with A) to 709 eV (labeled with B) is smaller than that of the reference spectrum of the hematite (not shown here), which is due to the existence of low chemical state of Fe such as Fe^{2+} (FeO or Fe$_3$O$_4$) in the hematite nanostructure because of the incomplete oxidation of ferrocene in the pyrolysis process.[15,36] It is also the reason for the formation of the carbon layer on the hematite nanostructure.[15] The sample after the first cycle exhibits an increased peak A and the ratio of peak A to peak B increases significantly, which strongly suggest the increase of the low chemical state of Fe^{2+} (FeO or Fe$_3$O$_4$).[36] In Fig. 4(c), the capacity decreases sharply after the first cycle. The irreversible capacity loss was attributed to irreversible processes such as electrolyte decomposition and the formation of

the SEI layer.[28,32] However, our XANES results reveal an increase of Fe^{2+} in the anode materials after the first cycle, and suggest that the anode materials are not completely restored to hematite (Fe^{3+}) after the delithiation process. Thus Li$^+$ ions can be trapped in the anode material along with the formation of Fe^{2+} and the capacity will decrease. It could be an important factor for the irreversible capacity after the first cycle except for the formation of the SEI layer along with further confirmation. Furthermore, XANES experiments confirm our hypothesis. The sample after 15 cycles also shows the existence of Fe^{2+} with a peak ratio of peak A to peak B decreased when compared to that after the first cycle, indicating the slow transformation from Fe^{2+} to hematite (Fe^{3+}) in the cycling process. The sample after 250 cycles shows a spectral shape with a strong peak B and a weak peak A, which can be attributed to fully transformed hematite (Fe^{3+}). The changes of Fe chemical state exhibit a good coordination with the capacity evolution.

More details about the composition evolution with cycling can be observed in the C K-edge and O K-edge XANES spectra. In Fig. 5(h), C K-edge XANES spectra of the anode materials are shown. The spectral intensities are proportional to the thickness or amount of carbon materials in the anode.[37] The curve for the sample before cycling shows a clear carbon signal but it is weak, indicating the existence of surface carbon coating on hematite, as revealed by TEM images. The curve for the sample after the first cycle also shows carbon signal with a slight increase of the intensity, which can be attributed to the electrolyte decomposition and the formation of the SEI layer. However, the carbon signal in the sample after 1 cycle is still weak, suggesting that the SEI layer is very thin. Thus the incomplete transformation of Fe could play a key role for the capacity loss.

The C K-edge XANES spectra for samples after 15 and 250 cycles are also shown in Fig. 5(h). The materials at C K-edge show different XANES spectra at different positions (part 1 and part 2). For the sample after 15 cycles, two typical parts by analyzing the STXM maps by pixel are identified and the distributions of the two components are labeled with green and red colors in Fig. 5(a), respectively. Fig. 5(b) shows the corresponding TEM image and Fig. 5(c) shows the magnified TEM image, indicated by a circle in Fig. 5(b). The XANES spectra at C K-edge for the two parts are shown in Fig. 5(h). The green curve (part 1, green in Fig. 5(a)) shows a weak carbon signal similar to that before cycling and after 1 cycle. However, the red curve (part 2, red in Fig. 5(a)) shows a strong carbon signal with a prominent feature at about 288.5 eV for oxidized carbon groups.[18,19] The strong carbon signal results from the cycling process by electrolyte decomposition. The capacity increase with cycling is common for hematite-based anodes, and it was attributed to the reversible growth of a polymeric gel-like film in literature.[28,30–32] Here, the existence of a strong carbon signal after 15 cycles can be arisen from the polymeric carbon film in the anode, which can also contribute to the capacity increase. Interestingly, the XANES spectrum for part 2 shows mainly oxidized carbon groups, whereas the signal for Li$_2$CO$_3$ at about 290.5 eV is very weak, suggesting that Li$_2$CO$_3$ is not the main composition in the SEI layer during the initial 15 cycles. For the sample after 250 cycles, two typical parts can be identified, labeled with green and red colors in Fig. 5(d). The XANES spectra at C K-edge for both parts show a strong carbon signal in Fig. 5(h), suggesting that after
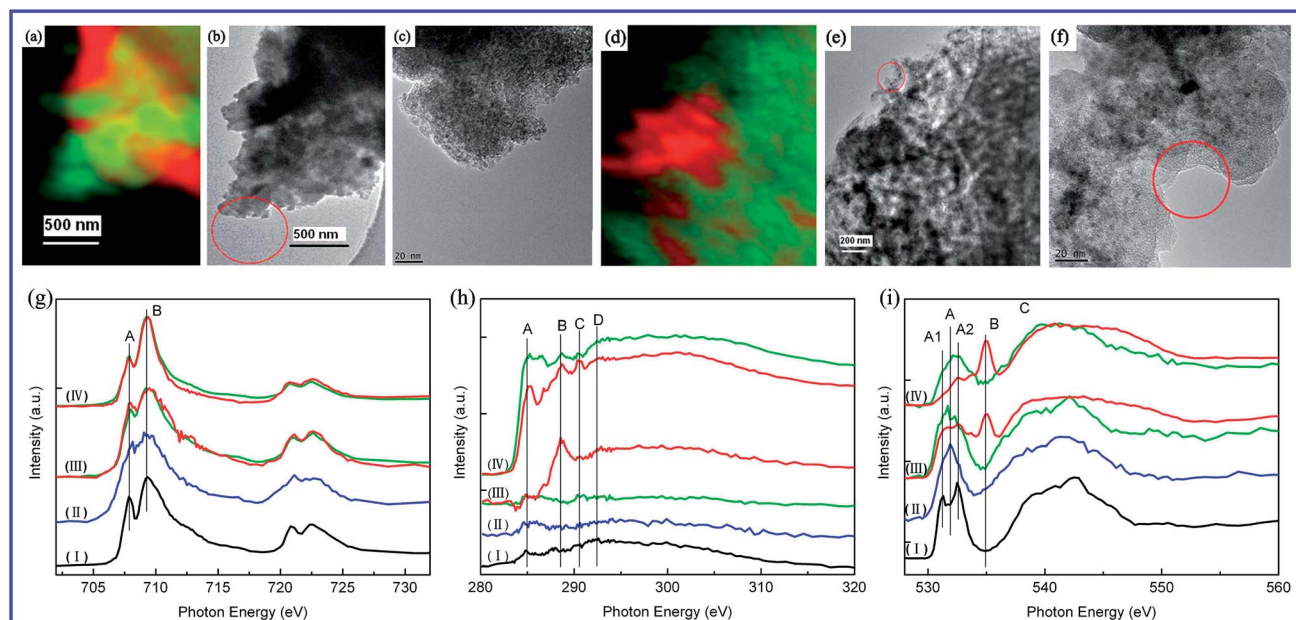
5186 | J. Mater. Chem. A, 2015, 3, 5183–5188

This journal is © The Royal Society of Chemistry 2015

Fig. 5 (a) STXM chemical map of the anode materials after 15 cycles (green: part 1, red: part 2), (b) corresponding TEM image of the same region and (c) magnified TEM image. (d) STXM chemical map of the anode materials after 250 cycles (green: part 1, red: part 2), (e) corresponding TEM image of the same region and (f) magnified TEM image. (g) Fe L-edge, (h) C K-edge and (i) O K-edge of XAS spectra of the anode materials (I) before cycling and (II), (III), (IV) after 1, 15, 250 cycles, respectively.

a long time cycling, the SEI layer becomes very thick. A feature at about 290.5 eV (feature C) for Li_2CO_3 can be found, suggesting a complicated composition after long time cycling.

The XANES spectra at O K-edge are shown in Fig. 5(i). The curve for the sample before cycling shows typical hematite features. The prepeaks can be attributed to transitions to anti-bonding O 2p states hybridized with the 3d metal states (t_{2g} and e_g orbital symmetry).[38,39] Feature C can be generally attributed to oxygen 2p states hybridized with iron 4s and 4p states.[38] The curve for the sample after 1 cycle shows a convolution of the prepeaks (A1 and A2), which stands for the presence of a low oxidation state of Fe such as Fe^0 or Fe^{2+}.[38] The XANES spectra at O K-edge confirm the existence of FeO or Fe_3O_4 in the anode after the first cycle. The XANES spectra for two parts of the sample after 15 cycles are also shown in Fig. 5(i). The green curve shows a spectral shape similar to that for the sample after 1 cycle with some FeO or Fe_3O_4, whereas the red curve shows an evidently different spectrum with a new peak B that stands for the formation of Li_2CO_3 or Li_2O.[40] C K-edge XANES spectrum for the same part reveals that there is only a very weak signal of Li_2CO_3, suggesting it is mainly Li_2O in this part. The prepeaks at about 532 eV for part 2 may come from hematite or Li_2O_2.[40] Thus the red part in Fig. 5(a) for the sample after 15 cycles mainly consists of carbon film (from the C signal), Li_2O and possible Li_2O_2. The sample after 250 cycles also shows two parts with similar spectra, as that after 15 cycles. The red curve shows the existence of Li_2CO_3 or Li_2O. The electrolyte decomposition in the first cycle leads to the formation of a thin SEI layer. Then, the SEI layer grows with cycling and Li_2O and Li_2O_2 can be observed. After long time cycling (such as 250 cycles), the carbon film is very thick and Li_2CO_3 and Li_2O are the final

products. Interestingly, from the STXM map in Fig. 5, we can find that Li_2CO_3, Li_2O, and the possible Li_2O_2 tend to aggregate to form islands instead of a uniform distribution.

Conclusions

We have presented a simple preparation of carbon-coated hematite to be used as the anode in LIBs. These anodes show a high reversible capacity of 1138 mA h g^{-1} after 300 cycles at a current density of 500 mA g^{-1}, and maintain a good capacity of 458.8 mA h g^{-1} even when cycled at a high current density of 10 000 mA g^{-1}. The high capacity can be attributed to the nanostructure and the coated carbon layer on hematite. Moreover, the working mechanism of the anode with cycling has also been probed by STXM, and a relationship between the Fe chemical state in the anode and the capacity evolution has been found, which shows that a low oxidation state of Fe (such as Fe^{2+}) might reduce the capacity by trapping Li^+ ions and the recovery of low oxidation state of Fe to hematite (Fe^{3+}) would significantly increase the capacity. STXM data also revealed that the detailed composition and electronic structure changes in the cycling process. The results show that the electrolyte decomposition in the first cycle led to the formation thin SEI layer, and the SEI layer grew with the presence of Li_2O and Li_2O_2. After a long time cycling (such as 250 cycles), the carbon film was very thick and Li_2CO_3 and Li_2O were the final products. Interestingly, from the STXM map, Li_2CO_3, Li_2O, and the possible Li_2O_2 are found to aggregate to form islands instead of a uniform film. The facile synthesis of carbon-coated α-Fe_2O_3 opens a good way for large-scale anode production in Li-ion

This journal is © The Royal Society of Chemistry 2015

J. Mater. Chem. A, 2015, **3**, 5183–5188 | **5187**

batteries, and the STXM study provides new insight into the mechanism of hematite-based Li-ion battery.

Acknowledgements

References

1 P. G. Bruce, B. Scrosati and J. M. Tarascon, *Angew. Chem., Int. Ed.*, 2008, **47**, 2930–2946.

2 Y. Luo, J. Luo, J. Jiang, W. Zhou, H. Yang, X. Qi, H. Zhang, H. J. Fan, D. Y. W. Yu, C. M. Li and T. Yu, *Energy Environ. Sci.*, 2012, **5**, 6559–6566.

3 Z. Wang, L. Zhou and X. W. Lou, *Adv. Mater.*, 2012, **24**, 1903–1911.

4 J. Chen, L. N. Xu, W. Y. Li and X. L. Gou, *Adv. Mater.*, 2005, **17**, 582–586.

5 J. S. Chen, T. Zhu, X. H. Yang, H. G. Yang and X. W. Lou, *J. Am. Chem. Soc.*, 2010, **132**, 13162–13164.

6 M. V. Reddy, T. Yu, C. H. Sow, Z. X. Shen, C. T. Lim, G. V. Subba Rao and B. V. R. Chowdari, *Adv. Funct. Mater.*, 2007, **17**, 2792–2799.

7 W. M. Zhang, X. L. Wu, J. S. Hu, Y. G. Guo and L. J. Wan, *Adv. Funct. Mater.*, 2008, **18**, 3941–3946.

8 Z. M. Cui, L. Y. Hang, W. G. Song and Y. G. Guo, *Chem. Mater.*, 2009, **21**, 1162–1166.

9 M. Zhou, T. W. Cai, F. Pu, H. Chen, Z. Wang, H. Y. Zhang and S. Y. Guan, *ACS Appl. Mater. Interfaces*, 2013, **5**, 3449–3455.

10 B. Zhang, Z. D. Huang, S. W. Oh and J. K. Kim, *J. Power Sources*, 2011, **196**, 10692–10697.

11 C. F. Zhang, X. Peng, Z. P. Guo, C. B. Cai, Z. X. Chen, D. Wexler, S. A. Li and H. K. Liu, *Carbon*, 2012, **50**, 1897–1903.

12 D. N. Wang, J. L. Yang, X. F. Li, D. S. Geng, R. Y. Li, M. Cai, T. K. Sham and X. L. Sun, *Energy Environ. Sci.*, 2013, **6**, 2900–2906.

13 E. K. Heidari, B. Zhang, M. H. Sohi, A. Ataie and J. K. Kim, *J. Mater. Chem. A*, 2014, **2**, 8314–8322.

14 A. Brandt and A. Balducci, *J. Power Sources*, 2013, **230**, 44–49.

15 J. J. Deng, X. X. Lv, J. Gao, A. W. Pu, M. Li, X. H. Sun and J. Zhong, *Energy Environ. Sci.*, 2013, **6**, 1965–1970.

16 B. J. Schultz, C. J. Patridge, V. Lee, C. Jaye, P. S. Lysaght, C. Smith, J. Barnett, D. A. Fischer, D. Prendergast and S. Banerjee, *Nat. Commun.*, 2011, **2**, 372–379.

17 J. G. Zhou, J. Wang, H. Liu, M. N. Banis, X. L. Sun and T. K. Sham, *J. Phys. Chem. Lett.*, 2010, **1**, 1709–1713.

18 J. Zhong, T. Xie, J. J. Deng, X. H. Sun, X. L. Pan, X. H. Bao and Z. Y. Wu, *Chem. Commun.*, 2011, **47**, 8373–8375.

19 A. Kuznetsova, I. Popova, J. T. Yates, M. J. Bronikowski, C. B. Liu, J. Huffman, R. E. Smalley, H. H. Hwu and J. G. G. Chen, *J. Am. Chem. Soc.*, 2001, **123**, 10699–10704.

20 X. S. Liu, J. Liu, R. Qiao, Y. Yu, H. Li, L. Suo, Y. S. Hu, Y. D. Chuang, G. Shu, F. Chou, T. C. Weng, D. Nordlund, D. Sokaras, Y. J. Wang, H. Lin, B. Barbiellini, A. Bansil, X. Song, Z. Liu, S. Yan, G. Liu, S. Qiao, T. J. Richardson, D. Prendergast, Z. Hussain, F. M. F. de Groot and W. L. Yang, *J. Am. Chem. Soc.*, 2012, **134**, 13708–13715.

21 S. L. Yang, D. N. Wang, G. X. Liang, Y. M. Yiu, J. J. Wang, L. J. Liu, X. L. Sun and T. K. Sham, *Energy Environ. Sci.*, 2012, **5**, 7007–7016.

22 J. G. Zhou, J. Wang, Y. F. Hu, T. Regier, H. L. Wang, Y. Yang, Y. Cui and H. J. Dai, *Chem. Commun.*, 2013, **49**, 1765–1767.

23 S. Graham and C. Fryhle, *Organic Chemistry*, John Wiley & Sons, Inc., USA, 9th edn, 2006.

24 B. Sun, J. Horvat, H. S. Kim, W.-S. Kim, J. Ahn and G. X. Wang, *J. Phys. Chem. C*, 2010, **114**, 18753–18761.

25 D. Larcher, C. Masquelier, D. Bonnin, Y. Chabre, V. Masson, J. B. Leriche and J. M. Tarascon, *J. Electrochem. Soc.*, 2003, **150**, A133–A139.

26 D. Larcher, D. Bonnin, R. Cortes, I. Rivals, L. Personnaz and J. M. Tarascon, *J. Electrochem. Soc.*, 2003, **150**, A1643–A1650.

27 J. Chen, L. N. Xu, W. Y. Li and X. L. Gou, *Adv. Mater.*, 2005, **17**, 582–586.

28 X. W. Li, L. Qiao, D. Li, X. H. Wang, W. H. Xie and D. Y. He, *J. Mater. Chem. A*, 2013, **1**, 6400–6406.

29 B. Wang, J. S. Chen, H. B. Wu, Z. Y. Wang and X. W. Lou, *J. Am. Chem. Soc.*, 2011, **133**, 17146–17148.

30 X. Wang, X. L. Wu, Y. G. Guo, Y. T. Zhong, X. Q. Cao, Y. Ma and J. N. Yao, *Adv. Funct. Mater.*, 2010, **20**, 1680–1686.

31 X. H. Wang, Z. B. Yang, X. L. Sun, X. W. Li, D. S. Wang, P. Wang and D. Y. He, *J. Mater. Chem.*, 2011, **21**, 9988–9990.

32 J. X. Zhu, Z. Y. Yin, D. Yang, T. Sun, H. Yu, H. E. Hoster, H. H. Hng, H. Zhang and Q. Y. Yan, *Energy Environ. Sci.*, 2013, **6**, 987–993.

33 B. B. Tian, J. Swiatowska, V. J. Maurice, S. Zanna, A. Seyeux, L. H. Klein and P. Marcus, *Langmuir*, 2014, **30**, 3538–3547.

34 B. L. Cushing and J. B. Goodenough, *Solid State Sci.*, 2002, **4**, 1487.

35 Y. J. Kwon and J. Cho, *Chem. Commun.*, 2008, **9**, 1109–1111.

36 E. de Smit, I. Swart, J. F. Creemer, G. H. Hoveling, M. K. Gilles, T. Tyliszczak, P. J. Kooyman, H. W. Zandbergen, C. Morin, B. M. Weckhuysen and F. M. F. de Groot, *Nature*, 2008, **456**, 222–225.

37 L. Bai, J. Wang, T. Xie, G. Zhao, J. Liu, J. Zhong and X. H. Sun, *J. Phys. Chem. C*, 2013, **117**, 1969–1973.

38 Z. Y. Wu, S. Gota, F. Jollet, M. Polllak, M. G. Soyer and C. R. Natoli, *Phys. Rev. B: Solid State*, 1997, **55**, 2570–2577.

39 A. Braun, K. Sivula, D. K. Bora, J. F. Zhu, L. Zhang, M. Grätzel, J. H. Guo and E. C. Constable, *J. Phys. Chem. C*, 2007, **116**, 16870–16875.

40 R. Qiao, Y. D. Chuang, S. Yan and W. Yang, *PLoS One*, 2012, **7**, e49182.